POLITECNICO DI TORINO
Repository ISTITUZIONALE

A new approach for displacement and stress monitoring of tunnel based on iFEM methodology

(Article begins on next page)

24 April 2024

ACCEPTED MANUSCRIPT

A new approach for displacement and stress monitoring of tunnel based on iFEM methodology

A new approach for displacement and stress monitoring of tunnel based on iFEM methodology

Pierclaudio Savino

Department of Structural, Geotechnical and building Engineering, Politecnico di Torino, Torino, Italy, pierclaudio.savino@polito.it, corresponding author.

Francesco Tondolo

Department of Structural, Geotechnical and building Engineering, Politecnico di Torino, Torino, Italy, francesco.tondolo@polito.it

Abstract. Structural monitoring plays a key role for underground structures such as tunnels. Strain readings are expected to report structural conditions during construction and at the final delivery of the works. Furthermore, it is increasingly requested an extension to long-term monitoring from contractors with possible use of the same system in service during construction. A robust and efficient monitoring methodology from discrete strain measurements is the inverse Finite Element Method (iFEM), which allows to reconstruct the structural response without input data on the load pattern applied to the structure as well as material and inertial properties of the elements and therefore it is interesting for structural configurations affected by uncertain loading conditions, such as the tunnel. The formulation presented in this paper, based on the iFEM theory, is improved from the previous work available in literature for both the shape functions used and the computational procedure. Indeed, the approach allows to overcome inconsistencies related to structural loading conditions and a pseudo-inverse matrix preserve all the rigid body modes without imposing specific constraints which is typical for tunnels. Numerical validation of the iFEM procedure is performed by simulating the input data coming from a tunnel working in a heterogeneous soil under different loading conditions with direct FEM analysis.

Keywords. iFEM, long-term monitoring, curved beam, shape sensing, tunnel, structural health monitoring.

1. Introduction

Underground constructions present an intrinsic level of complexity caused by the interaction with natural environment in civil engineering problems and they are then affected by multiple uncertainties since the choice of design assumptions to the end of their service life. Unlike surface constructions in which materials with well-known properties are gradually assembled to build a structure that finds its equilibrium in the desired final configuration, underground constructions are built in a pre-existing equilibrium under unknown conditions. The pre-existing stresses within the ground before the excavation is modified by the opening of a cavity and channelling around it creating the "arch effect". An important task of a tunnel design engineer that affects the integrity and life of a tunnel is to determine the proper stresses and how trigger the arch effect by calibrating excavation and stabilisation operations. Furthermore, lateral and transversal deformations of tunnel structures may occur during service life due to geotechnical activities which leads to stress variation in structural members. In this context, the monitoring is a fundamental tool for the current tunnelling practice that takes part in the construction phases and throughout its service life. In the first time it allows to verify the accuracy of the input parameter predicted and then to fine tune the design by adjusting the stabilisation operations and calibrating the rate of tunnelling. Once the structure is completed, it is also important to check the conditions over time, especially in relation to the rheological and hydrogeological conditions [1]. Long-term monitoring can also help to reduce uncertainties in the decision-making process by establishing triggering thresholds that exceed specific structural performance levels. Until a few years ago monitoring during service life of the tunnel was not very common, due to the interference with service. The current trend is to equip the structure with remote measurement transmission systems.

A conventional method used for monitoring tunnels is the convergence measurement. The method relies on the distances between couple of points inside the tunnel done with optical measures. Due to the intermittent recordings, interrupting construction operations and the impossibility to apply the technique to survey tunnel stability during service, the extensometric technique, installing electric strain gages on the internal steel arches of any tunnel support system [2]. This technology requires the installation of a number of transversal and longitudinal devices to check in some points the internal strains to be compared with design

1

values. Therefore, only a local comparison with expected data is available. With the rapid development of fiber optic sensing technology, distributed fiber optic sensor (FOS) has been applied to tunnels. Barbosa et al. [3] proposed an automatic tunnel monitoring system using a metallic profile instrumented with FOS and installed on the tunnel surface. Tunnel convergences are estimated with the mathematical model by Gama [2] which allows to model the radial displacements starting from the initial point achieved by topographic calibration. MacPherson et al. [4] presented a multiplexed fibre Bragg grating strain sensor in a multicore fibre, fixed across the join between tunnel lining sections. Wang et al. [5] introduced a new package with an additional plastic tube in the middle part of the sensor to prevent the FOS from unbonding with the Basalt fiber. Inaudi and Walder [6] presented the application of distributed FOS to detect in a highway tunnel strains and cracks of concrete lining due to hydrostatic pressure, in a railway tunnel the increase of knowledge on the structural behaviour between tunnel lining and the vertical support columns and in a penstock tunnel the discovery micro-cracks in the welds caused by a landslide. To improve the understanding and prediction on the response of the existing tunnel due to close boring activities, Gue et al. [7] presented a case study on the monitoring with distributed FOS of an existing cast iron tunnel during the construction of Crossrail's platform tunnel. De Battista et al. [8] used a distributed FOS embedded within the sprayed concrete lining to monitor strains on the tunnel lining, during the excavation of cross-passages. Other monitoring methods refer to different techniques such as laser scanning. To understand the tunnel behaviour between the construction phase and the final stabilized shape, Nuttens et al. [9] proposed the application of terrestrial laser scanning for ovalization measurements from the ring assembly until three months after construction. Considering that the relative spatial relationship between each segment of the lining ring agrees with the variation of the inclination of each segment, Zhang et al. [10] obtained the variation of tunnel diameter using wireless inclinometers. A technique based on tunnel deformation monitoring system using ultrasonic transducers has been proposed by Sheng Xu et al. [11]. Experimental tests highlighted the dependence by probe angles, distances and surrounding temperature variations and then the need of suitable coefficients compensating the deviations. As railway tunnels are usually long in the longitudinal direction, a reliable monitoring method using a wireless sensor network was developed by Tsuno and Hirata [12]. A SHM network with crackmeters and inclinometers has been deployed in a road tunnel in Italy, to understand the non-linear interaction with the slow-moving landslide [13]. Due to the difficulties to make a quantitative evaluation for the long-term safety using analytic method, Wang et al. [14] developed a multi-level fuzzy synthetic evaluation model.

Although there are applications that allow to employ SHM by defining an alarm threshold level, still many application limits and computational approximations need to be overcome. In strain sensing techniques in which the fibre optic is glued on the lining surface, extra care should be taken during installation due to their fragility; many applications require the occupation of the roadway and some sensors can only provide limited number of measuring points. From the computational point of view, analysis carried out by Mohamad et al. [15] underlined the importance of measuring also the axial strain in the tunnel ring and subtracting it to calculate the actual deflection of the lining as a result of bending. Embedded sensor in tunnel lining and therefore axial strain as well as bending strain need to be detected. The advances in the Micro Electro-Mechanical System (MEMS) field have made possible embedded systems that allow to reconstruct the entire deformed shape of complex structures with use of a large number of low-costs strain sensors [16]. Experimental test on a concrete beam reinforced with steel bars incorporating barometric pressure sensor in appropriate sealed cavities showed the robustness of the system during construction and loading phase [17].

An algorithm particularly effective for SHM, that allows to reconstruct the entire deformed shape of a structure starting from a limited number of strain measurements, was developed by Tessler and Spangler [18] in the aeronautical field; it is also known as inverse Finite Element Method (iFEM). The present shape-sensing methodology also implies that other crucial quantities such as stresses can be evaluated, thus enabling real-time damage prediction. The formulation, based on a least-squares variational principle, allows to reconstruct the response of a discretized structural domain without relying on mechanical and loading knowledge. Because only strain-displacement relations are involved, solely strains and geometric measurements are required. Specialized by Gherlone et al. [19] for the shape sensing of truss, beam and frame structures with Timoshenko behaviour, the theory was applied for civil engineering field by Savino et al. [20], with a formulation according to the kinematical assumptions of the Bernoulli-Euler theory. Indeed, in order to make this computational

2

method available also to reconstruct the deformed shape of curved elements, Savino et al. [21] developed the theory according to the kinematic assumptions of Bernoulli-Euler curved beam theory including the membrane and bending deformations. The inverse curved element, formulated with bi-quintic polynomials, is able to provide an adequate representation of rigid-body motions and locking-free behaviour. Kefal et al. [22] proposed a new iFEM formulation to model laminated composite and sandwich plates and shells with a three-node inverse-shell element named i3-RZT. The linear incremental iFEM procedure has been introduced by Tessler et al. [23] to reconstruct the displacement field of a shell structure undergoing geometric nonlinearity. Furthermore, the application of the iFEM theory not only involved the full-field displacements and stress-strain reconstruction but also the detection of possible damage locations. Colombo et al. [24] used the iFEM algorithm to create a load-adaptive baseline for damage identification based on an anomaly index. Roy et al. [25] introduced the use of the iFEM to localize damages by reconstructing the damaged strain field of the structure. Mathematical concepts have been also demonstrated with experimental application to SHM of aerospace, marine and mechanical structures. Gherlone et al. [26] considering a laboratory experiment on a thin-walled cantilevered beam, investigated the accuracy of the deformed shape reconstructed by strain-rosette data by comparison with displacement transducers measurements. Kefal and Oterkus [27] performed displacement and stress monitoring of a typical chemical tanker mid-ship based on iFEM methodology. Papa et al. [28] validated the iFEM formulation with the Mindlin plate on a wing of an unmanned aircraft vehicle properly equipped with strain gages. Since the deformation of the gantry structure in heavy-duty machine tools is an important factor that affects machining accuracy, Liu et al. [29, 30] verified the accuracy of the iFEM algorithm with fiber Bragg grating sensors in the mechanical manufacturing field. Niu et al. [31] presented a multi-nodes iFEM that reconstructs the displacement of a flexible antenna panel consistent with Mindlin plate theory.

Due to the independency by the type of construction methods and loading pattern coming from geological and hydrogeological conditions, the use of iFEM is particularly effective in the tunnel monitoring. In this paper, further developments of the computational method are presented to make it suitable also for the underground structures. Despite satisfactory results of bi-quintic shape functions, a new highly efficient shape functions have been designed to overcome numerical inefficiencies; this incorporates an adequate representation of the possible rigid-body or strain-free motions other than the strain-inducing motions. To obtain the exact solution, the governing differential equations of Bernoulli-Euler curved beam have been solved, taking into account the coupling between radial and circumferential displacement. A further novelty is introduced in the present formulation because the inverse solution for tunnel static scheme does not provide for specifying problem-dependent displacement boundary conditions. To solve the latter problem, the Moore-Penrose pseudoinverse matrix [32-33] is employed. This matrix is frequently used to solve a system of linear equations when the system does not have a unique solution or has many solutions. The method relies on the singular value decomposition (SVD) to form a system of linear equations. The resulting singular system of algebraic equations that allow to calculate the unknown degrees of freedom can be then efficiently solved providing the deformed structural-shape predictions.

After a comparison between two types of shape functions, the case of a bored tunnel under a flat and a slope terrain is presented. In order to simulate measured strains on field, the results of a finite element analysis using PLAXIS 2D software [34] are used.

2. Inverse Finite Element Method for curved beam

The deformations of curved iFEM elements are assumed to correspond to the assumptions of Bernoulli-Euler theory [21]. The geometry of the generic element can be suitably described introducing the curvilinear coordinates (R, β), which gives the curvilinear abscissa (Fig. 1) with the following derivative:
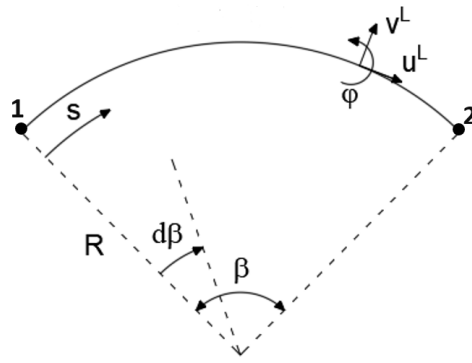
$$ds = R \cdot d\beta$$

3

Figure 1 - Curved beam geometry.

The displacement field is completely defined by the radial displacement v, tangential displacement u and the rotation φ. The kinematic variables can be interpolated within the element using a set of shape functions $N(\beta)$,

$$u(\beta) = N(\beta) \cdot u^e$$

where u^e are the nodal degrees of freedom. According to the adopted structural theory, the strain field can be expressed in terms of nodal degrees of freedom

$$e(u) = B(\beta) \cdot u^e \tag{1}$$

where the matrix $B(\beta)$ contains the derivatives of the shape functions $N(\beta)$. The iFEM approach reconstructs the deformed shape of a discretized structure by minimizing a functional Φ defined as the least-squares error between experimental section strains obtained by in situ strain measurements, e^ε, and analytic section strain, $e(u)$. For a single element, the error functional is expressed by

$$\Phi^e(u) = \left\| e(u) - e^\varepsilon \right\|^2$$

Thus, in case of discretization with m elements, the total lest-squares functional is the sum of each one

$$\Phi = \sum_{e=1}^{m} \Phi^e$$

Accounting for the membrane and bending deformations, the squared norms can be written in terms of the normalized Euclidean norms such as

$$\left\| \varepsilon(u) - \varepsilon^\varepsilon \right\|^2 = \frac{L^e}{n} \cdot \sum_{i=1}^{n} (\varepsilon(\beta_i) - \varepsilon_i^\varepsilon)^2$$

$$\left\| \chi(u) - \chi^\varepsilon \right\|^2 = \frac{I^e L^e}{A^e n} \cdot \sum_{i=1}^{n} (\chi(\beta_i) - \chi_i^\varepsilon)^2$$

where L^e, A^e and I^e are the length of the element, the area and the moments of inertia, n is the number of locations where the section strains are evaluated.

The minimization of the inverse-element error functional with respect to the unknown nodal dof u^e leads to the inverse element matrix equation:

$$[S^e] \cdot \{u^e\} = \{h^e\}$$

where the matrix $[S^e]$ and the vector $\{h^e\}$ can be split in the membrane, ε, and flexural, χ, contributions:

$$[S_\varepsilon^e] = \frac{L^e}{n} \sum_{i=1}^{n} \{B_\varepsilon(\beta_i)\}^T \{B_\varepsilon(\beta_i)\}$$

$$[S_\chi^e] = \frac{I^e L^e}{A^e n} \sum_{i=1}^{n} \{B_\chi(\beta_i)\}^T \{B_\chi(\beta_i)\}$$

4

$$\{h_\varepsilon^e\} = \frac{l^e}{n} \sum_{i=1}^{n} \{B_\varepsilon(\beta_i)\}^T \varepsilon_{o_i}^\varepsilon$$

$$\{h_\chi^e\} = \frac{I^e \, L^e}{A^e \, n} \sum_{i=1}^{n} \{B_\chi(\beta_i)\}^T \chi_i^\varepsilon$$

The usual finite element assembly of a discretized structure, taking into account coordinate transformations to the global coordinate systems, is then performed giving a linear system of algebraic equations:

$$[S] \cdot \{u\} = \{h\}$$

Since the matrix [S] contains the rigid body motion of the structure, it is a singular matrix and the prescription of displacement boundary conditions is essential to get the inverse. However, there are applications for which all rigid body motions are unrestrained and then the inverse of rank deficient matrix should be computed. This study widens the previous foundings on iFEM analysis by taking the inverse of the symmetric matrix [S] without eliminating the rigid body components. Moore and Penrose showed that there is a general solution to theses equations by taking into account the Moore-Penrose "pseudo-inverse" $[S^\dagger]$, which is the unique matrix that satisfies the following four properties:

$$S \cdot S^\dagger \cdot S = S$$

$$S^\dagger \cdot S \cdot S^\dagger = S^\dagger$$

$$(S \cdot S^\dagger)^T = S \cdot S^\dagger$$

$$(S^\dagger \cdot S)^T = S^\dagger \cdot S$$

Further, the Moore-Penrose inverse $S^\dagger$ yields the inverse S^{-1} when S is square and a non-singular matrix. When S is not full rank and then have nor eigenvalue and eigenvector, the pseudo-inverse can be computed using the Singular Value Decomposition (SVD). Then there exist orthogonal matrices U and V such that the matrix S can be decomposed as follows:

$$S = U \cdot \Sigma \cdot V^T$$

where Σ is a matrix having the form:

$$\Sigma = \begin{vmatrix} \sigma_1 & 0 & \cdots & 0 & 0 \\ 0 & \sigma_2 & \cdots & 0 & 0 \\ \vdots & \vdots & \cdots & \vdots & \vdots \\ 0 & 0 & \cdots & 0 & 0 \\ 0 & 0 & \cdots & \sigma_p & 0 \end{vmatrix}$$

and $\{\sigma_i\}$ are the singular values of the matrix S found from the non-zero eigenvalues of $S^T \cdot S$ and $S \cdot S^T$. The columns of the orthogonal matrices U and V are respectively the left singular vectors and the right singular vectors. Using the SVD of the matrix S, the pseudo-inverse of this matrix can be computed from the following equation:

$$S^\dagger = V \cdot \Sigma^\dagger \cdot U^T$$

where the matrix $\Sigma^\dagger$ takes the form:

$$\Sigma^\dagger = \begin{vmatrix} 1/\sigma_1 & 0 & \cdots & 0 & 0 \\ 0 & 1/\sigma_2 & \cdots & 0 & 0 \\ \vdots & \vdots & \cdots & \vdots & \vdots \\ 0 & 0 & \cdots & 0 & 0 \\ 0 & 0 & \cdots & 1/\sigma_p & 0 \end{vmatrix}$$

If the matrix S is rank deficient, then one or more of its singular values will be zero and is placed in the corresponding entry of $\Sigma^\dagger$.

5

With the pseudo-inverse matrix $[S^\dagger]$, the least squares solution for the inverse problem lacks of a unique displacement field and is computed by:

$$\{u\} = [S^\dagger] \cdot \{h\} \tag{2}$$

In line with traditional iFEM solution, Eq. 2 is suitable for real time monitoring because $[S^\dagger]$ remains unchanged for a given distribution of strain sensors; the vector $\{h\}$ needs to be updated during each strain-data acquisition. Using the evaluated vector of unknown dof $\{u\}$, the continuous strain field of the structure can be obtained through the derivatives of the shape functions (Eq. 1). Furthermore, the stresses are computed using constitutive relations and can be introduced into appropriate failure criteria for damage prediction.

3. High efficiency shape functions for curved element

A key step of the iFEM formulations is the definition of suitable shape functions. The definition of the shape functions for curved elements consider the representation of the rigid body mode, the membrane-bending coupling, the membrane-shear locking, etc. To achieve a good accuracy and convergence property, two factors should be taken into account in the model definition:

- the element displacement field must contain a proper representation of any rigid-body motion;
- to represent all possible strain-modes accurately, the displacement components should contain at least as many terms as the exact solutions of the differential Euler equations which govern the behaviour of the element.

Nevertheless, it has been widely recognized in literature that good results could be reached without the explicit representation of the rigid-body motions but only adopting independently-interpolated displacement at least of fifth degree. A bi-quintic inverse element was introduced by Savino et al. [21] for iFEM formulation obtaining fast convergence in terms of displacements. However, the use of polynomial displacement function could leads to issues in stability of the solution [35]. Due to this reason, new high-efficiency shape functions (HESF) for an exact representation of the rigid-body motions are proposed. To satisfy such requirements, the coupling between normal and tangential displacements should be taken into account by analytically solving the strain-displacement equations of the curved beam theory. Ashwell et al. [35] showed how to derive satisfactory shape function from simple assumed strain functions, $f_\varepsilon(\beta)$ and $f_\chi(\beta)$, by integrating the strain-displacement equations

$$\varepsilon = \frac{1}{R}\left(\frac{du}{d\beta} + v\right) = f_\varepsilon(\beta)$$

$$\chi = \frac{1}{R^2}\left(-\frac{du}{d\beta} + \frac{d^2v}{d\beta^2}\right) = f_\chi(\beta) \tag{3}$$

where the number of independent constants in, $f_\varepsilon(\beta)$ and $f_\chi(\beta)$, has been chosen considering six degrees of freedom for an element.

In this work new high-efficiency shape functions have been obtained, increasing the terms of polynomial functions according to the twelve degrees of freedom adopted in Savino et al. [21] to define the bi-quintic inverse element (Fig. 2)

$$\{u^e\} = \{u_1, u'_1, u''_1, v_1, v'_1, v''_1, u_2, u'_2, u''_2, v_2, v'_2, v''_2\}^T$$
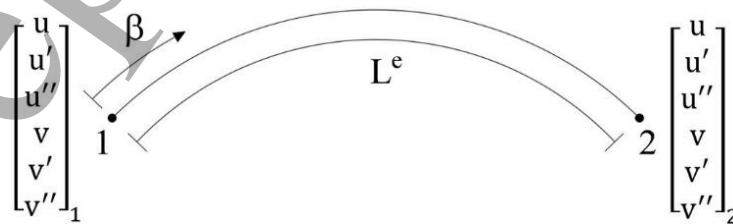

Figure 2 - Two node inverse finite element (Savino et al. [21]).

To obtain the equations that represent the rigid-body displacements with zero deformations, the solution of the associated homogeneous system ($f_\varepsilon(\beta) = f_\chi(\beta) = 0$) must be calculated, resulting:

$$v_0 = c_1 \cos(\beta) + c_2 \sin(\beta)$$

6

$$u_0 = -c_1 \sin(\beta) + c_2 \cos(\beta) + c_3 \tag{4}$$

A suitable choice for $f_\varepsilon(\beta)$ and $f_\chi(\beta)$ is required, to accurately represent the strain state inherent the circumferential deformation, ε, and the increase in curvature, χ. The arch element has twelve degrees of freedom and consequently the shape functions should have twelve independent constants. Among these constants, three are required for the rigid-body motions (Eq. 4), leaving the remaining nine for the strain functions

$$f_\varepsilon = c_4 + c_5\beta + c_6\beta^2 + c_7\beta^3$$

$$f_\chi = c_8 + c_9\beta + c_{10}\beta^2 + c_{11}\beta^3 + c_{12}\beta^4 \tag{5}$$

By substituting Eq. 5 into Eq. 3, the following particular integrals are obtained

$$v_p = c_4 R + c_5 R \beta + c_6 (R \beta^2 - 2 R) + c_7 (R \beta^3 - 6 R \beta) + c_8 R^2 + c_9 R^2 \beta + c_{10}(R^2 \beta^2 - 2 R^2) + c_{11}(R^2 \beta^3 - 6 R^2 \beta) + c_{12}(24 R^2 - 12 R^2 \beta^2 + R^2 \beta^4)$$

$$u_p = c_6 2 R \beta + c_7 3 R \beta^2 - c_8 R^2 \beta - c_9 \frac{R^2\beta^2}{2} + c_{10}\left(2 R^2 \beta - \frac{R^2\beta^3}{3}\right) + c_{11}\left(3 R^2 \beta^2 - \frac{R^2\beta^4}{4}\right) + c_{12}\left(4 R^2 \beta^3 - 24 R^2 \beta - \frac{R^2\beta^5}{5}\right) \tag{6}$$

The general equations of the displacement field result by adding the solution of the associated homogeneous (Eq. 4) and of the particular integral (Eq. 6). The polynomials thus calculated contain the explicit representation of the rigid-body motions and the coupling of the displacement field. The shape functions are obtained after calculating the twelve independent constants by imposing the boundary conditions on the element's nodes. In this way, the issues related to the use of polynomial displacement functions in the form reported by Savino et al. [21] are solved.

4. Numerical study

4.1 Comparison between bi-quintic and high efficiency shape function

In order to demonstrate the numerical performance of the shape functions introduced in the previous paragraph from the point of view of both the displacement and strain field, a comparison with the bi-quintic shape function [21] is reported. To simulate experimentally measured strains and to obtain reference displacements, direct FEM analysis with LUSAS software [36] is performed using a refined mesh of 20 elements with Bernoulli-Euler shape functions. The element used is a parabolically curved beam in which the tangential and radial displacements are approximated along the length as quadratic and cubic functions, respectively.

A configuration of deep-thick semi-arch, clamped on one side and free on the other is studied having a curved beam with radius of curvature $R = 1$ m, opening angle $\beta = 90°$ and rectangular cross section with $b = 0.3$m and $h = 0.5$m. The beam is modelled in direct FEM analysis with linear elastic isotropic material of Young's modulus $E = 210$ GPa and Poisson's ration $\upsilon = 0.3$. The comparison is performed with reference to two loading conditions: a concentrated tip force ($F = 1$ KN) and a uniformly distributed load ($q = 10$ KN/m) (Fig. 3 a-b).
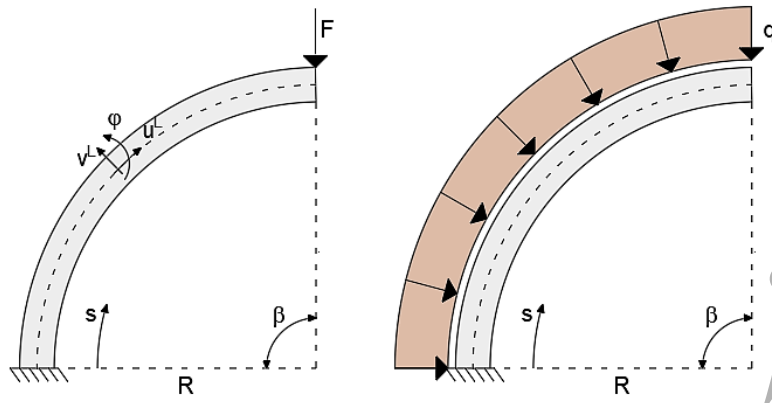
Figure 3 – The deep-thick arch: a) concentrated force, b) distributed load.

For both cases, the beam is modelled in the iFEM analysis using only one inverse element restrained with the boundary conditions described above and five station points spaced by 22.5° (Fig. 4).
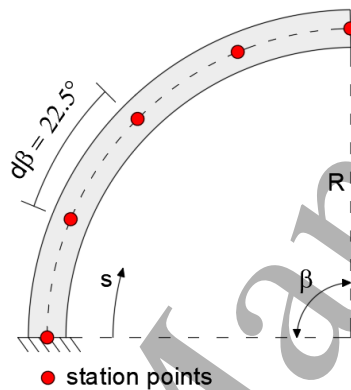

● station points

Figure 4 – Inverse finite element.

The displacements and strains (continuous lines) are compared with those obtained by FEM analysis depicted with the red dots in Figures 5-6. As expected, in both cases (Fig. 5 (a-b) concentrated force, Fig. 6 (a-b) distributed load) a good agreement is registered for displacements and deformation, except for the fluctuations obtained in the axial deformations in case of using the bi-quintic shape functions.
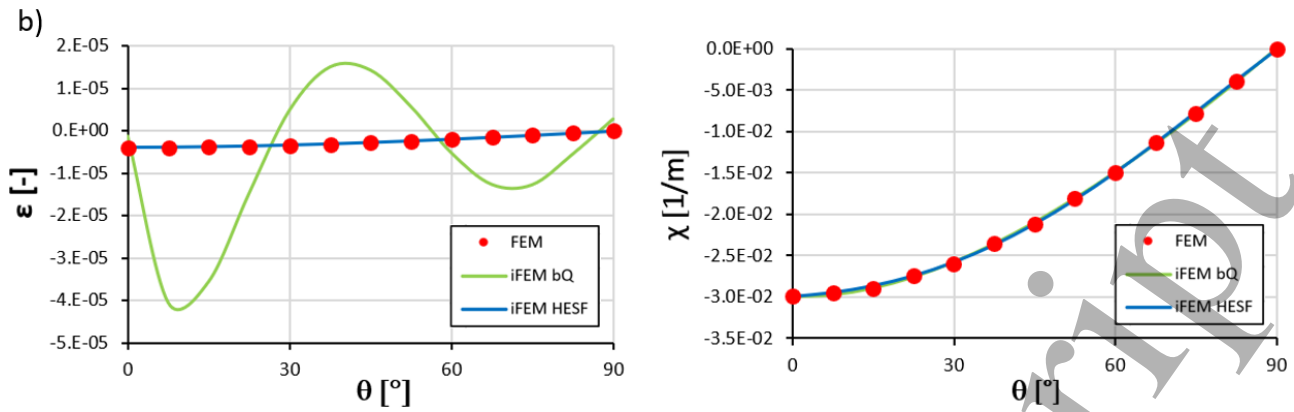
a)
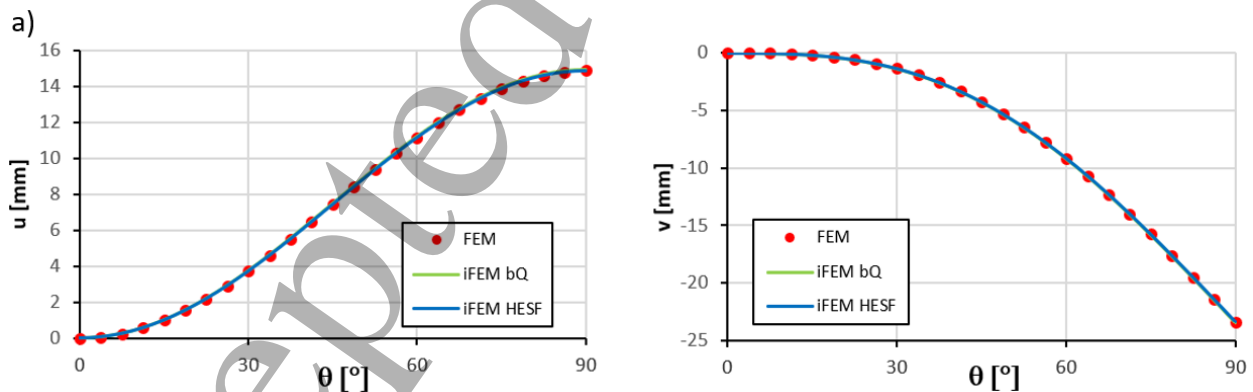
Figure 5 – Comparison between iFEM (bi-quintic and HESF) and FEM solutions for concentrated force: a) u and v displacements, b) ε and χ strain.
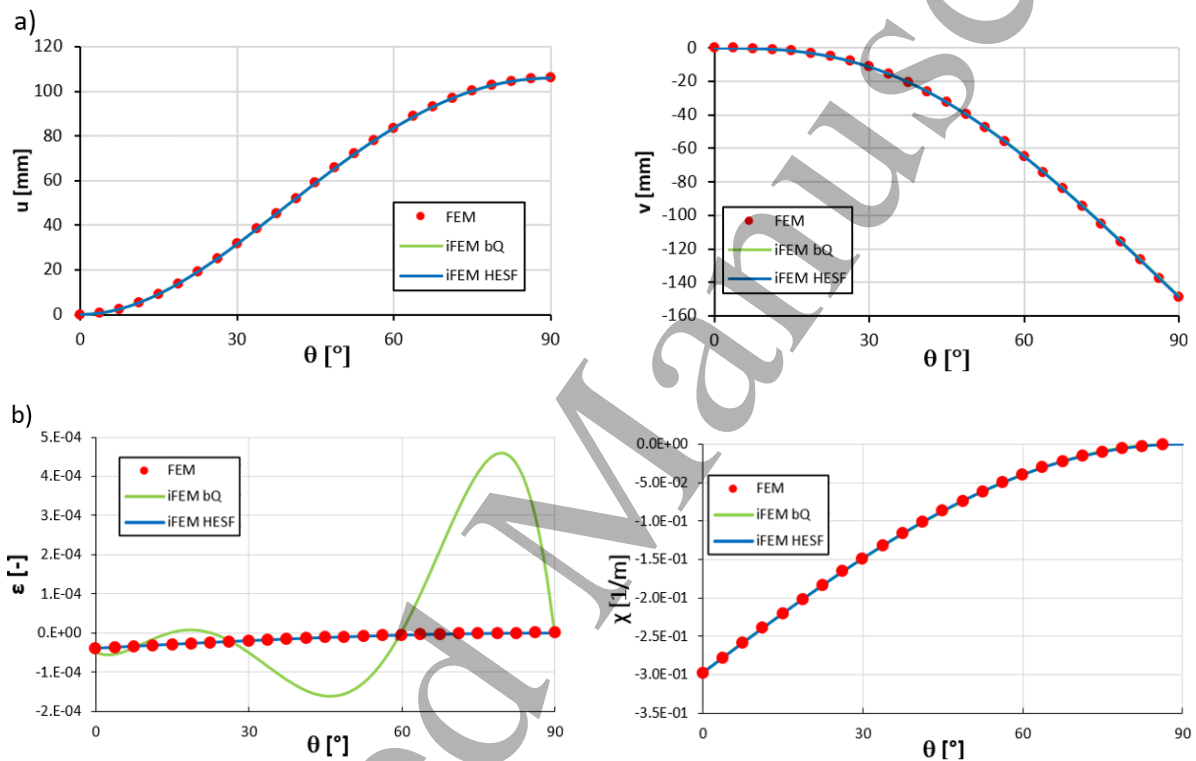

Figure 6 – Comparison between iFEM (bi-quintic and HESF) and FEM solutions for distributed load: a) u and v displacements, b) ε and χ strain.

As showed above, a high improvement in performance has been achieved with the new shape functions in terms of strain outcome.

4.2 Real case study

The application of the iFEM method integrated with the pseudo-inverse matrix and the new inverse curved beam element is tested simulating the cases of a bored tunnel under a flat and a slope terrain. Direct FEM analyses, performed using PLAXIS 2D [34], are used to provide both input strain measurements and data as reference results for iFEM analyses. The tunnel segment is modelled using one-dimensional curved element with three degrees of freedom per node: two translational and one rotational. Each beam element is defined by 5 nodes whereas 15-node soil elements are used to model the soil behavior. The lining is discretized with a total of 12 elements.

The tunnel has a diameter of 8 m and its centre is located at a depth of 14 m. The soil profile related to the flat configuration, contains the first layer with a thickness of 7 m and consists of clay. Below there are two layers with thickness of 7 m respectively, in which the tunnel is located. The first one is modelled as sand whereas the remaining part is deep sand. The mechanical behaviour of soil is modelled with linear-elastic-perfectly-

9

plastic Mohr-Coulomb law with the parameters listed in Table 1. The further layer below is considered to be fully rigid and modelled by appropriate boundary conditions. All boundaries are restrained according to the Standard fixities provided by the PLAXIS 2D toolbar, i.e. fully fixity at the base of the geometry and roller conditions at the vertical sides (Fig. 7).
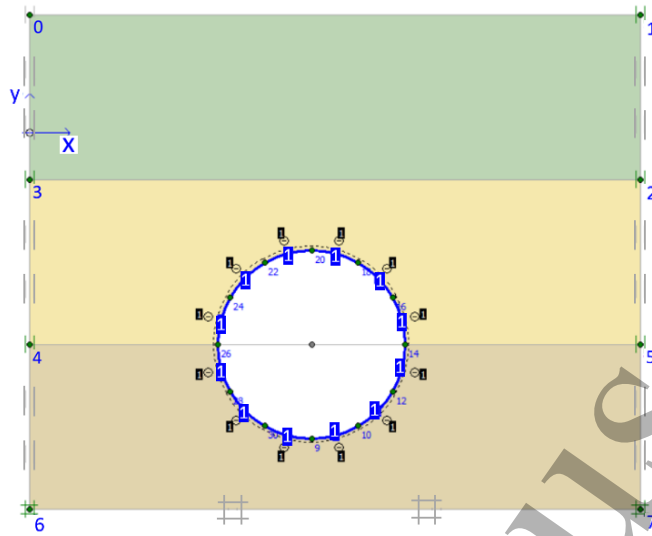

Figure 7 - Geometry of the tunnel project with the soil layers (flat land).

	Clay	**Sand**	**Deep Sand**
γ_{unsat} [KN/m^3]	15	16.5	17
E [KN/m^2]	3400	80000	120000
υ	0.33	0.3	0.3
c [KN/m^2]	5.5	1	1
φ [°]	24	31	33

Table 1 - Material properties of soil.

The tunnel lining is modelled with curved beams of normal stiffness EA = $1.4 \cdot 10^7$ [KN/m], flexural rigidity EI = $1.43 \cdot 10^5$ [KNm^2/m], thickness d = 0.35 [m] and Poisson's ratio υ = 0.15.

The accuracy of the iFEM prediction is assessed by means of the average percentage difference between the predicted parameters, x^{iFEM}, and the experimentally simulated ones coming from FEM analysis, x^{FEM}, given as:

$$\%e_{Diff,x} = \frac{100}{n} \sum_{i=1}^{n} \frac{x_i^{iFEM} - x_i^{FEM}}{x_{max}^{FEM}} \qquad (16)$$

where x indicates the data analysed and n the number of the output points. The effectiveness of the shape functions in converging to the correct solution, is also examined by plotting the number of inverse elements used to model the structure, against the average percentage difference.

Regular mesh patterns are used having each inverse curved element with the minimum number of station points [21]. The strain sensors configurations consist of five station points referred at the centroid axes and equally spaced along the element (red dots). As depicted in Fig. 8, the tunnel is modelled with 2, 3 and 4 inverse curved elements numbered internally with subtended angle (β) of 180°, 120° and 90° respectively (beginning and end of each element is evidenced by a transversal segment).
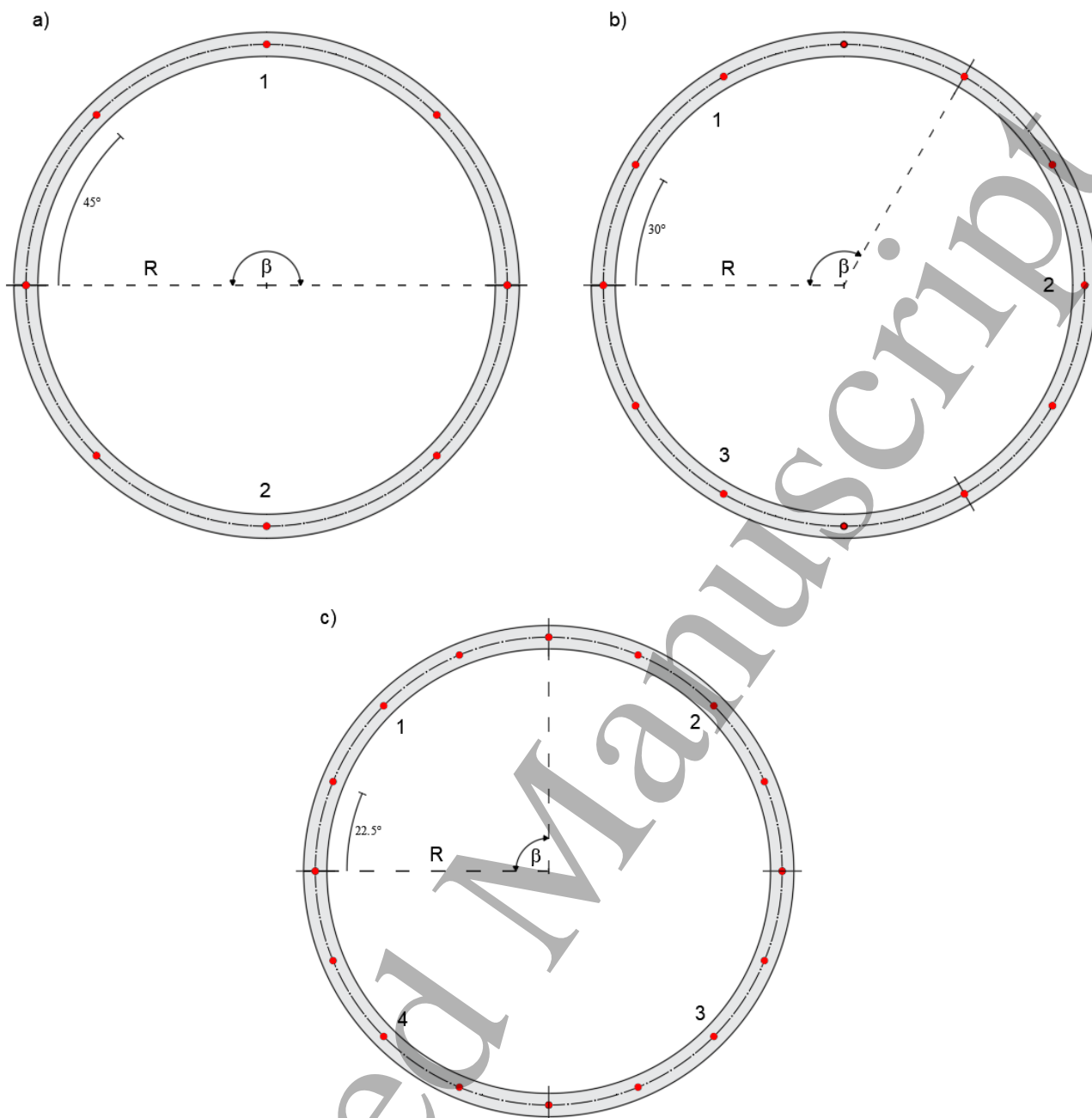
10

Figure 8 - Strain sensors configurations: a) 2 inverse elements, b) 3 inverse elements, c) 4 inverse elements.

To demonstrates the accuracy of the iFEM approach and the effectiveness of the increasing number of inverse elements used, Fig. 9 shows the comparison between the strain state obtained via FEM and three iFEM configurations. The influence on the results of both the number of inverse elements and the station points is studied. Accurate results have been obtained using a minimum number of three inverse elements and twelve station points.
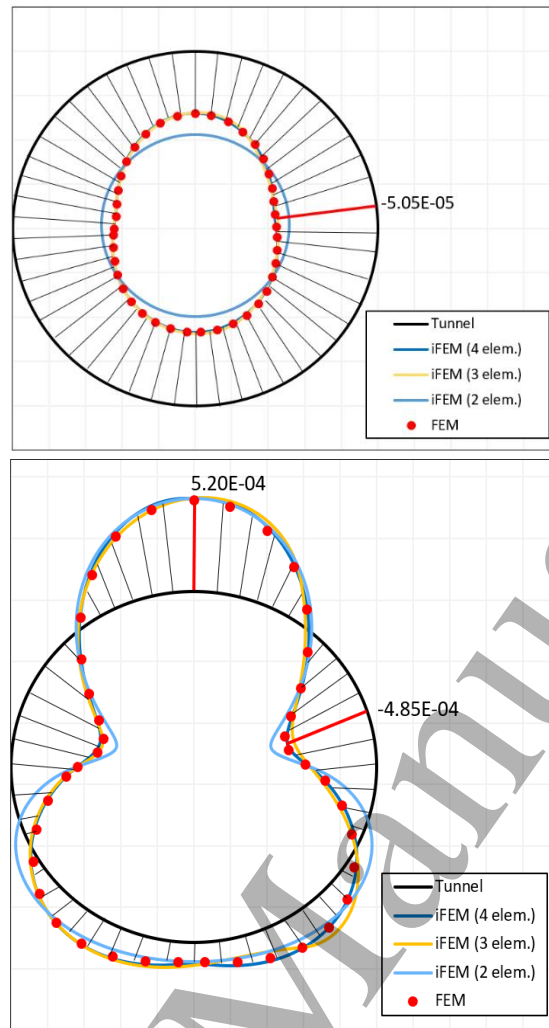
11

Figure 9 - Comparison along the beam axis of iFEM solution to FEM strain state (flat land).

The possibility to reconstruct the whole strain field allows to know other quantities such as stresses that can be obtained using constitutive laws. A convergence analysis has been performed to evaluate the adequacy of the new high-efficiency shape functions (Fig. 10).
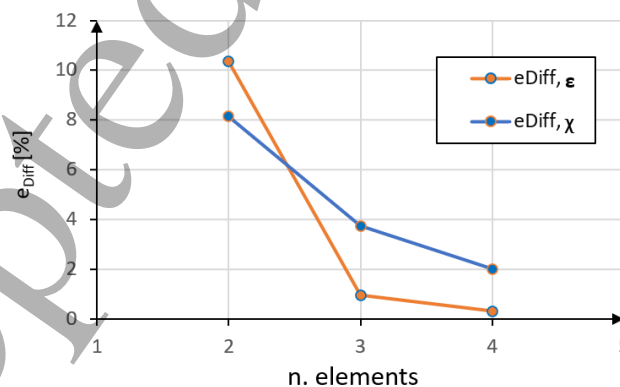

Figure 10 - Convergence diagram: average percentage difference vs. number of inverse elements.

Figure 10 depicts the convergence of the average percentage difference according to the number of inverse elements used in the modelling; particularly for the discretization with four inverse elements, the error on the membrane strain is 0.32% while that on the flexural strain is 2.02%.

12

The same material properties and tunnel geometry have been adopted to model the case of a bored tunnel in presence of slope. In this case the first layer has a variable thickness from a minimum of 2 m to a maximum of 7 m (Fig. 11).
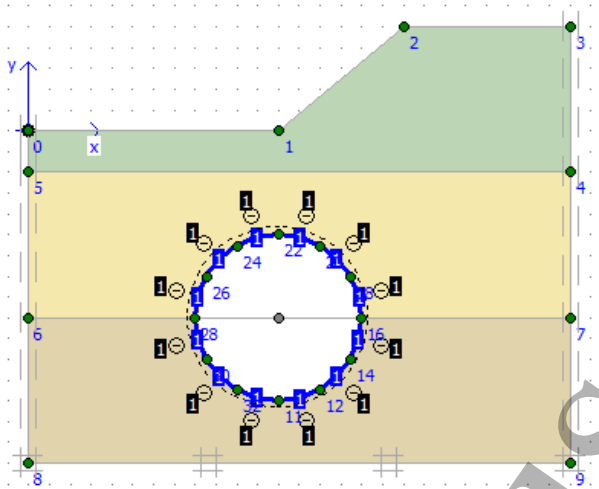

Figure 11 - Geometry of the tunnel project with the soil layers (slope land).

In Fig. 12 the accuracy of the iFEM approach in terms of strain distribution along the beam element for the bored tunnel with slope is demonstrated. Again, to evaluate the influence of the number of both sensors used and inverse elements, three different configurations have been considered (Fig. 8).

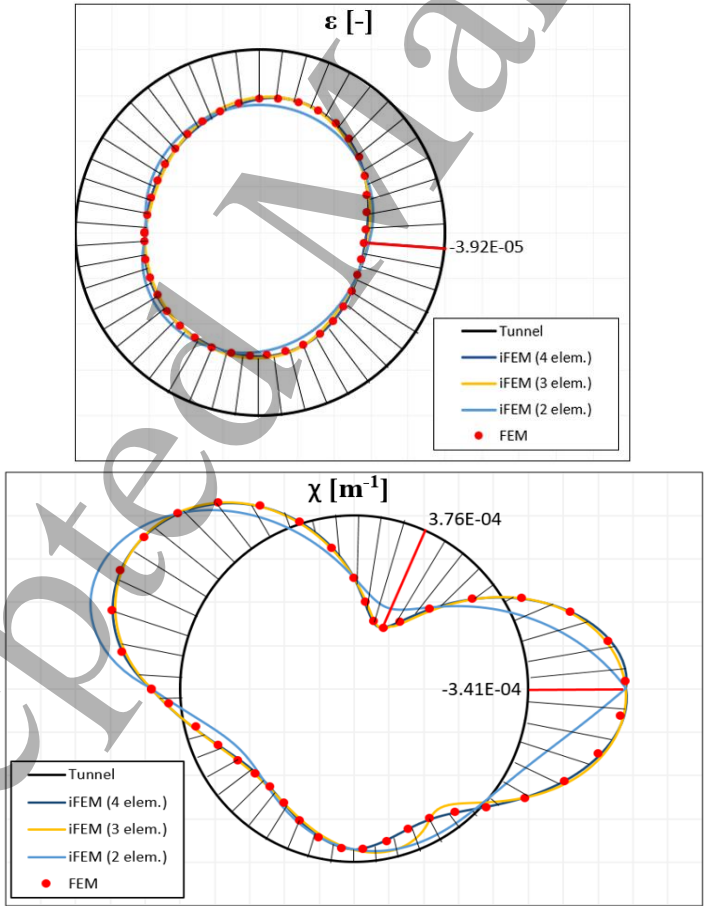*Figure 11 - Comparison along the beam axis of iFEM solution to FEM strain state (slope land).*

Figure 13 depicts the convergence analysis of the average percentage difference according to the number of inverse elements used in the modelling; particularly for the discretization with four inverse elements, the error on the membrane strain is 0.65% while that on the flexural strain is 0.90%.
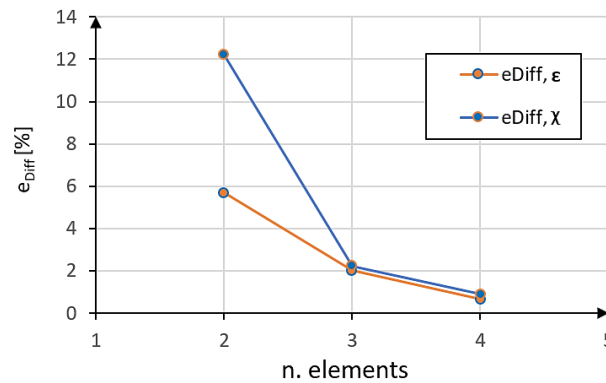
13

Figure 12 - Convergence diagram: average percentage difference, vs. number of inverse elements.

The results obtained demonstrate the accuracy of the iFEM approach with the pseudo-inverse matrix, integrated with the new shape functions. Despite the problem complexity, a good agreement is reached between the FEM and iFEM predictions with a relatively limited number of strain sensors.

Conclusions

In order to establish a suitable computational method for the structural health monitoring system in tunnel application, a new formulation have been implemented in the inverse Finite Element Method (iFEM). The present shape sensing methodology has relevant implications for the monitoring of smart structures equipped with discrete strain sensors, resulting an enabling technology to provide feedback to the control system. The reconstruction of the full-field displacement allows to obtain key quantities of structural response and to monitor in real-time the safety level. The iFEM uses a least-squares variational principle involving membrane and bending deformations of Bernoulli-Euler curved beam theory. The error functional enforces the compatibility between experimentally measured strains and strains interpolated within the inverse elements in a least-squares sense.

The Moore-Penrose inverse matrix is introduced to solve the issue in analysing singular and rank deficient matrix deriving by the typical configuration of tunnel structures characterized by unrestrained rigid-body. The pseudoinverse matrix is obtained from the Singular Value Decomposition tool, inverting all singular non-zero values.

A new inverse element, having two node and twelve degrees of freedom, have been developed. The element shape functions are based on the analytical solution of the strain-displacement equations of the curved beam theory to take into account the coupling between normal and tangential displacements. The formulation shows effectiveness in terms of both strain and displacement outcomes by comparison with bi-quintic shape functions based on interdependent interpolations previously developed [21].

The shape-sensing capability have been demonstrated simulating a case study of a tunnel in a heterogeneous soil and subject to an asymmetrical load. To provide the simulated and reference measurements, a finite element analysis has been developed using PLAXIS 2D code. The iFEM has shown to be highly effective and efficient in predicting the structural response.

Future efforts will concern the assessment of the algorithm efficiency in case of noise related to real measurements that affect experimental data. For such purpose, a greater number of station points than the minimum required in iFEM formulation with a proper signal processing could be necessary. Similar approach could be used in case of potential malfunctioning of sensors due to the harsh environment that can be also overcome with a new configuration of the inverse elements and the relative position of the station points along each element.

Conflicts of interest

The authors declare that there is no conflict of interest.

REFERENCES

[1] Lunardi P. Design and Construction of Tunnels: Analysis of controlled deformation in rock and soils (ADECO-RS). Berlin: Springer; 2008.

[2] Dinis da Gama C. A method for continuous monitoring of tunnel deformations during construction and service phases. Eurock'2004, Austria.

[3] Barbosa C, Malva R, Silva A, Moretti G, Suzuki D, Goncalves L. Automatic monitoring system for continuous structural assessment of tunnels: application results and insights. Proc World Tunn Congr 2014, Brazil.

[4] MacPherson WN, Silva-Lopez M, Barton JS, Moore AJ, Jones JDC, Zhao D, et al. Tunnel monitoring using multicore fibre displacement sensor. Meas Sci Technol. https://doi.org/10.1088/0957-0233/17/5/S41

[5] Wang T, Shi B, Zhu Y. Structural monitoring and performance assessment of shield tunnels during the operation period, based on distributed optical-fiber sensors. Symmetry, https://doi.org/10.3390/sym11070940.

[6] Inaudi D, Walder R. Full-length tunnel structural monitoring. Structural Health Monitoring 2019, https://doi.org/10.12783/shm2019/32293.

[7] Gue CY, Wilcock M, Alhaddad MM, Elshafie MZEB, Soga K, Mair RJ. The monitoring of an existing cast iron tunnel with distributed fibre optic sensing (DFOS), J Civil Structural Health Monitoring 2015, https://doi.org/10.1007/s13349-015-0109-8.

[8] de Battista N, Elshafie M, Soga K, Williamson M, Hazelden G, Hsu YS. Strain monitoring using embedded distributed fibre optic sensors in a sprayed concrete tunnel lining during the excavation of cross-passages. 7th Int Conf Structural Health Monitoring Intell Infrastructure (SHMII7) 2015, Torino, Italy.

[9] Nuttens T, Stal C, Backer HD, Schotte K, Bogaert PV, Wulf AD. Methodology for the ovalization monitoring of newly built circular train tunnels based on laser scanning: Liefkenshoek Rail Link (Belgium). Automation in Construction 2014, https://doi.org/10.1016/j.autcon.2014.02.017.

[10] Zhang J, Liu W, Zhao M. The real-time monitoring system for metro shield tunnels: from research to application. 7th Eur workshop on structural health monitoring 2014, Nantes, France.

[11] Sheng Xu D, Meng Zhao Y, Bei Liu H, Hu Zhu H. Deformation monitoring of metro tunnel with a new ultrasonic-based system. Sensors 2017, https://doi.org/10.3390/s1708175.

[12] Tsuno K, Hirata R. Tunnel monitoring method based on wireless sensor network. Q Rep of RTRI 2014, https://doi.org/10.2219/rtriqr.55.27.

[13] Bossi G, Schenato L, Marcato G. Structural health monitoring of a road tunnel intersecting a large and active landslide. Appli Sci 2017, https://doi.org/10.3390/app7121271.

[14] Wang B, Mo C, He C, Yan Q. Fuzzy synthetic evaluation of the long-term health of tunnel structures. Appl Sci 2017, https://doi.org/10.3390/app7020203.

[15] Mohamad H, Soga K, Bennett PJ, Mair RJ, Lim CS. Monitoring twin tunnel interaction using distributed optical fiber strain measurements. J Geotec Geoenviron Eng 2012, https://doi.org/10.1061/(ASCE)GT.1943-5606.0000656.

[16] Tondolo F, Cesetti A, Matta E, Quattrone A, Sabia D. Smart reinforcement steel bars with low-cost MEMS sensors for the structural health monitoring of RC structures. Construction Build Mater 2018, https://doi.org/10.1016/j.conbuildmat.2018.04.045.

[17] Tondolo F, Matta E, Quattrone A, Sabia D. Experimental test on an RC beam equipped with embedded barometric pressure sensors for strains measurement. Smart Mater Struct 2019, https://doi.org/10.1088/1361-665X/ab1172.

[18] Tessler A, Spangler JL. A variational principle for reconstruction of elastic deformation of shear deformable plates and shell. NASA TM-2003-212445, Hampton, VA, USA.

[19] Gherlone M, Cerracchio P, Mattone M, Di Sciuva M, Tessler A. Shape sensing of 3D frame structures using an inverse Finite Element Method. Int J Solid Struct 2012, https://doi.org/10.1016/j.ijsolstr.2012.06.009.

[20] Savino P, Gherlone M, Tondolo F. Shape sensing with inverse finite element method for slender structure. Struct Eng Mech 2019, https://doi.org/10.12989/sem.2019.72.2.217.

[21] Savino P, Gherlone M, Tondolo F, Tessler A. Application of Inverse Finite Element Method to Shape Sensing of Curved Beams. Sens 2020, https://doi.org/10.3390/s20247012.

[22] Kefal A, Tessler A, Oterkus E. An enhanced finite element method for displacement and stress monitoring of multilayered composite and sandwich structures. Comp Str 2017, doi:10.1016/j.compstruct.2017.07.078

[23] Tessler A, Roy R, Esposito E, Surace C, Gherlone M. Shape Sensing of Plate and Shell Structures Undergoing large Displacements Using the Inverse Finite Element Method. Shock Vib 2018, doi:10.1155/2018/8076085

[24] Colombo L, Sbarufatti C, Giglio M. Definition of a load adaptive baseline by inverse finite element method for structural damage identification. Mech Sys Sign Proc 2019. doi:10.1016/j.ymssp.2018.10.041

[25] Roy R, Gherlone M, Surace C. Damage Localisation in Thin Plates Using the Inverse Finite Element Method. Proc of 13th Int Conf Dam Assess Str 2020, Singapore.[26] Gherlone M, Cerracchio P, Mattone M, Di Sciuva M, Tessler A. Beam shape sensing using inverse finite element method: theory and experimental validation. Proc of 8th Int Work Str Heal Monit 2011, Stanford, California.

[27] Kefal A, Oterkus E. Displacement and stress monitoring of a chemical tanker based on inverse finite element method. Oc Eng 2016, doi:10.1016/j.oceaneng.2015.11.032

[28] Papa U, Russo S, Lamboglia A, Del Core G, Iannuzzo G. Health structure monitoring for the design of an innovative UAS fixed wing through inverse finite element method (iFEM). Aer Sci Tech 2017, doi:10.1016/j.ast.2017.07.005.

[29] Liu M, Zhang X, Song H, Wang J, Zhou S. Reconstruction algorithm for obtaining the bending deformation of the base of heavy-duty machine tool using inverse finite element method. Metrol Meas Syst 2018, doi:10.24425/mms.2018.124878.

[30] Liu M, Zhou F, Song H, Yang X, Wang J. Deformation Reconstruction for a Heavy-Duty Machine Column Through the Inverse Finite Element Method. IEEE Sens J 2020. doi:10.1109/JSEN.2020.2989139.

[31] Niu S, Li K, Liu J, Bao H. A Refined Shape Sensing Method for Skin Antenna Structure Based on Inverse Finite Element Method. Appl Sci 2020, doi:10.3390/app10217620.

[32] Moore EH. On the reciprocal of the general algebraic matrix. Bull Am Math Soc 1920, 26, 394-395.

[33] Penrose R. A generalized inverse for matrices. Math Proc Camb Philos Soc 1955, https://doi.org/10.1017/S0305004100003040.

[34] Brinkgreve RBJ. Plaxis: finite element code for soil and rock analyses: 2D – Version 8: [user's guide]. 2002.

[35] Ashwell DG, Sabir AB, Roberts TM. Further studies in the application of curved finite elements to circular arches. Int J Mech Sci 1971, https://doi.org/10.1016/0020-7403(71)90038-5.

[36] LUSAS Finite Element System V15.1(1995) User Manual, UK: FEA Ltd; 1995.

16